The separatrix electron density in JET, ASDEX Upgrade and Alcator C-Mod H-mode plasmas: A common evaluation procedure and correlation with engineering parameters

D. Silvagni[1*], O. Grover[1], A. Stagni[2], J. W. Hughes[3], M. A. Miller[3], B. Lomanowski[4], G. Ciraolo[5], M. Dunne[1], T. Eich[6], L. Frassinetti[7], C. Giroud[8], I. Jepu[8], A. Kallenbach[1], A. Kirjasuo[9], A. Kuang[6], T. Luda[1], C. Perez von Thun[10], T. Pütterich[1], H. J. Sun[8], H. Zohm[1], the ASDEX Upgrade team[a], JET contributors[b] and the EUROfusion tokamak exploitation team[c]

[1] *Max-Planck-Institut für Plasmaphysik, 85748 Garching, Germany*
[2] *Consorzio RFX (CNR, ENEA, INFN, Università di Padova, Acciaierie Venete SpA), Corso Stati Uniti 4, 35127 Padova, Italy*
[3] *MIT Plasma Science and Fusion Center, Cambridge, MA, USA*
[4] *Oak Ridge National Laboratory, Oak Ridge, TN 37831-6169, USA*
[5] *IRFM, CEA, St. Paul-Lez-Durance, France*
[6] *Commonwealth Fusion Systems, Devens, Massachusetts 01434, USA*
[7] *Division of Electromagnetic Engineering and Fusion Science, KTH Royal Institute of Technology, Stockholm, Sweden*
[8] *CCFE, Culham Science Centre, Abingdon, OX14 3DB, UK*
[9] *VTT, PO Box 1000, FI-02044 VTT Espoo, Finland*
[10] *Institute of Plasma Physics and Laser Microfusion, Hery 23, 01-497 Warsaw, Poland*
[a] *See author list of H. Zohm et al, 2024 Nucl. Fusion https://doi.org/10.1088/1741-4326/ad249d*
[b] *See author list of C. F. Maggi, 2024 Nucl. Fusion https://doi.org/10.1088/1741-4326/ad3e16*
[c] *See author list of E. Joffrin et al., 2024 Nucl. Fusion https://doi.org/10.1088/1741-4326/ad2be4*

Abstract

The separatrix electron density is an important parameter for core-edge scenario integration in tokamak devices, as it influences plasma confinement, divertor detachment and disruption avoidance. This quantity has been measured in H-mode discharges on JET, ASDEX Upgrade and Alcator C-Mod by applying the same fitting function to Thomson scattering measurements, and by employing the same analysis technique based on scrape-off layer power balance. To estimate the power crossing the separatrix, the inter-ELM time derivative of the plasma energy $\mathrm{d}W/\mathrm{d}t$ has been experimentally evaluated and found to be approximately a constant fraction of the absorbed heating power. Correlations between $n_{e,\mathrm{sep}}$ and engineering parameters have been investigated, revealing that $n_{e,\mathrm{sep}}$ scales with the divertor neutral pressure $p_{0,\mathrm{div}}$ in a similar manner across all devices. Additionally, when $n_{e,\mathrm{sep}}$ is normalized to the obtained $p_{0,\mathrm{div}}$ dependency, no clear correlation with the plasma current is found. These observations are in agreement with the 2-point model, which suggests that the upstream separatrix density is mainly set by the recycling at the divertor target.

Preprint submitted to Nuclear Materials and Energy *January 8, 2025*

1. Introduction

One of the major – and still open – key challenges on the pathway to a fusion power plant based on the tokamak concept is the integration of a high confinement scenario (H-mode) with a power and particle exhaust solution, typically achieved via divertor detachment. This needs to be reached while avoiding plasma disruptions, i.e. sudden losses of plasma temperature and current which are extremely harmful for the tokamak assembly and the plasma facing components. Interestingly, both H-mode confinement and divertor detachment strongly depend on the separatrix electron density, $n_{e,\mathrm{sep}}$, with high $n_{e,\mathrm{sep}}$ favoring detachment [1, 2, 3] and reducing confinement in some cases [4, 5, 6, 7]. Furthermore, the separatrix density is also a crucial parameter setting the stability of MARFEs and hence leading to plasma disruption [8, 9, 10]. Therefore, in order to find a proper core-edge integrated scenario solution, it is important to improve our quantitative prediction capabilities of $n_{e,\mathrm{sep}}$ and to advance our understanding of the basic physics processes setting such a parameter.

Several theoretical and experimental studies highlighted the importance of scrape-off layer (SOL) and divertor physics in determining the upstream $n_{e,\mathrm{sep}}$ via the so-called two-point model [11, 12, 13, 14, 15]. In particular, $n_{e,\mathrm{sep}}$ can be expressed as a function of different engineering parameters (such as plasma current, toroidal magnetic field, machine size etc.) and of the electron temperature or ion flux at the outer divertor target. Kallenbach et al. [15] related the target ion flux to the divertor neutral pressure $p_{0,\mathrm{div}}$, expressing $n_{e,\mathrm{sep}}$ as a function of engineering parameters only. Indeed, $p_{0,\mathrm{div}}$ can be regarded as an engineering parameter in devices with a closed divertor and active pumping. However, all these previous studies focused on single tokamaks, and a multi-machine database would be required to challenge the 2-point model dependencies, in particular the role of machine size.

A multi-machine investigation of the separatrix parameters is a challenging task from the experimental point of view. First, it requires high-resolution diagnostics able to measure temperature and density profiles with sufficient accuracy in the steep gradient region of all devices. Then, it needs edge profiles fitting being carried out with the same methodology. And lastly, the separatrix position needs to be defined in a consistent way across devices. Unfortunately, magnetic equilibrium reconstruction could exhibit a considerable error around the separatrix. Therefore, a typical technique used to estimate the separatrix position is SOL power balance, assuming that most of the SOL parallel heat flux is transported by electron conduction [16]. This methodology allows estimation of the separatrix temperature with reduced error, due to the strong temperature dependence of electron conductivity [17]. However, the power-balance estimated separatrix strongly depends on the model inputs, which are not always consistently chosen across different research groups.

In this work, we present a multi-machine database of H-mode plasmas where separatrix data have been assembled with exactly the same procedure across three different tokamaks: JET, ASDEX Upgrade (AUG) and Alcator C-Mod (C-Mod). In section 2, the main features

*Corresponding author
Email address: davide.silvagni@ipp.mpg.de (D. Silvagni[1])

of the database are described, along with the common methodology used to evaluate the separatrix temperature and density. In section 3, we present a sensitivity analysis of the obtained separatrix data on different inputs: The inter-ELM time derivative of the plasma stored energy, $\mathrm{d}W/\mathrm{d}t$, the SOL power decay length λ_q, and the SOL connection length between the outer midplane and the outer target, L_{SOL}. In section 4, $n_{e,\mathrm{sep}}$ correlations with engineering parameters such as the divertor neutral pressure and plasma current are presented. Lastly, in section 5, the main conclusions are outlined.

2. Database characteristics and separatrix position evaluation

The database is composed of 236 H-mode plasma phases in lower single null configuration and with a closed divertor geometry. The JET database is a subset of the EUROfusion pedestal database [18], where discharges have been down-selected to be in the so-called vertical-vertical (VV) target divertor configuration (see Fig. 1) and to have stationary sub-divertor neutral pressure. The discharges are all unseeded and ELMy H-modes. The AUG database consists of H-mode discharges previously analyzed in [15], which include both ELMy and no-ELM phases, with seeded and unseeded plasmas. The C-Mod database is a subset of two databases [19, 20] which have been also down-selected to have plasmas with a similar closed divertor configuration (see Fig. 1) and stationary sub-divertor neutral pressure. The C-Mod discharges considered here are unseeded and consist of EDA H-modes, i.e. there are no ELMs.

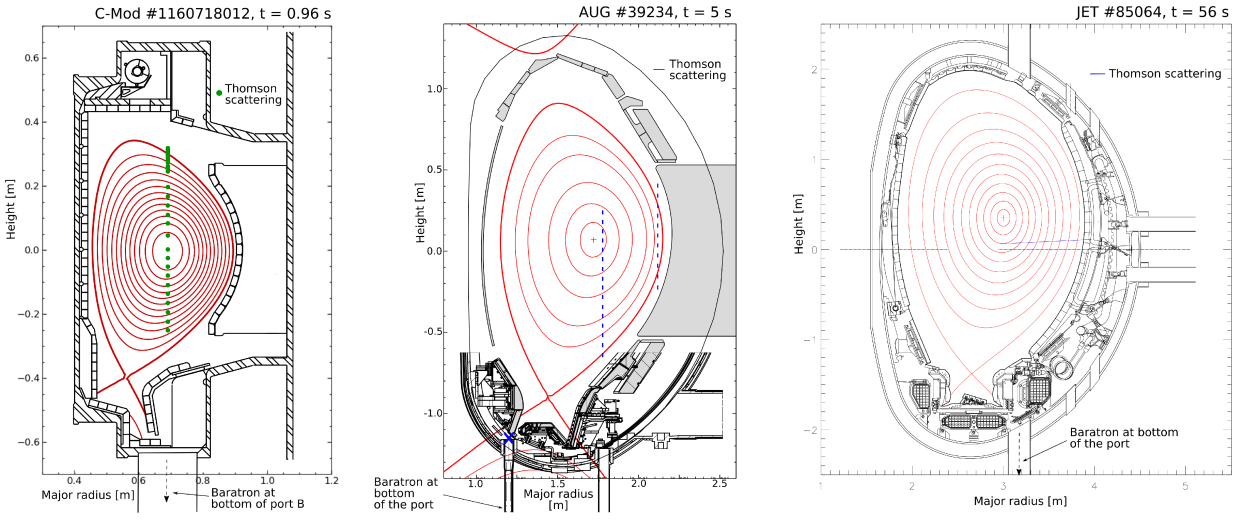

Figure 1: Poloidal cross-section of the vessel and a typical plasma equilibrium in C-Mod (left), AUG (center) and JET (right). The measurement location of the Thomson scattering system and baratron is indicated for each device. In AUG, a turbomolecular pump located at the end of the high-field-side vertical port causes a pressure drop along the pipe. For this reason, baratron measurements in AUG are calibrated to represent the pressure at the port entrance (blue cross). In C-Mod and JET, no substantial pressure drop is expected within the pipe.

	C-Mod	AUG	JET
Discharges	101	43	92
I_p (MA)	0.6–1.4	0.6–1.2	1.5–2.6
B_t (T)	4.5–7.8	1.8–2.6	2.1–3.3
q_{95}	2.9–7.2	3.1–6.9	2.9–4.2
P_SOL (MW)	0.5–2.5	0.7–12.8	4.9–18.8
$\overline{n}_e$ (10^{19} m^{-3})	16.9–53.6	4.8–13.2	3.6–10.1
δ_av	0.4–0.5	0.2–0.4	0.2–0.4
κ	1.5–1.7	1.5–1.7	1.6–1.8

Table 1: Parameter range of the assembled database.

The main plasma parameters of the assembled database are summarized in table 1. A wide range of plasma current (I_p), on-axis toroidal magnetic field (B_t), edge safety factor (q_{95}), line-averaged density ($\overline{n}_e$), and power entering the SOL (P_SOL) is obtained. In terms of plasma shape, the elongation (κ) and the average triangularity ($\delta_\mathrm{av} = (\delta_\mathrm{low} + \delta_\mathrm{up})/2$) also exhibit a considerable variation. Compared to next-generation devices [21, 22, 23], while B_t, q_{95}, $\overline{n}_e$ and plasma shape span most of the expected values, I_p and P_SOL are substantially lower.

In this study, $P_\mathrm{SOL} = P_\mathrm{abs} - P_{r,\mathrm{sep}} - \mathrm{d}W_\mathrm{MHD}/\mathrm{d}t$, where P_abs is the absorbed heating power, $P_{r,\mathrm{sep}}$ is the radiated power within the separatrix and $\mathrm{d}W_\mathrm{MHD}/\mathrm{d}t$ is the time derivative of the plasma stored energy evaluated from equilibrium reconstruction. In ELMy H-modes, $\mathrm{d}W_\mathrm{MHD}/\mathrm{d}t$ has been evaluated in the inter-ELM phase under analysis, see section 2.1.

The absorbed heating power is defined as $P_\mathrm{abs} = P_\mathrm{ohm} + P_\mathrm{aux}$, where P_ohm is Ohmic heating power and P_aux is the sum of all absorbed auxiliary heating powers. In AUG and JET, the main auxiliary heating system is neutral beam injection (NBI), and the power absorbed by the confined plasma is calculated subtracting losses due to charge exchange reactions, first ion orbit losses and shine-through. In JET, NBI shine-through is evaluated using the PENCIL code [24], while charge exchange and first orbit losses are estimated using an approximate formula [25, 26]. In AUG, these losses are evaluated using regression laws derived from a large database of TRANSP simulations [27]. These losses represent a small fraction of P_abs (1.5 % in JET and 1.9 % in AUG on average); therefore, using approximate formulas have minimal impact on the results of this work. In C-Mod, the auxiliary power is supplied by ion cyclotron resonance heating (ICRH), and is defined as $P_\mathrm{aux} = \eta_\mathrm{ICRH} P_\mathrm{ICRH}$, where P_ICRH is the ICRH power launched from the antenna and η_ICRH represents the fraction of power absorbed by the confined plasma. This C-Mod dataset includes two heating schemes: D(H) minority heating at low magnetic field ($B_t \sim 5.4\,\mathrm{T}$) and D(He^3) minority heating at high magnetic field ($B_t \sim 7.8\,\mathrm{T}$). The fraction of absorbed ICRH power is assumed to be 0.8 for D(H) heating and 0.5 for D(He^3) heating, consistent with the mean absorption values observed in similar plasma conditions [28, 29].

The radiated power within the separatrix is evaluated differently on each machine. In AUG and JET, tomographic reconstruction of line-integrated measurements from resistive bolometers is used [30, 31]. In cases where tomographic reconstruction is unavailable at JET, an alternative method based on a weighted average of wide bolometer channels from

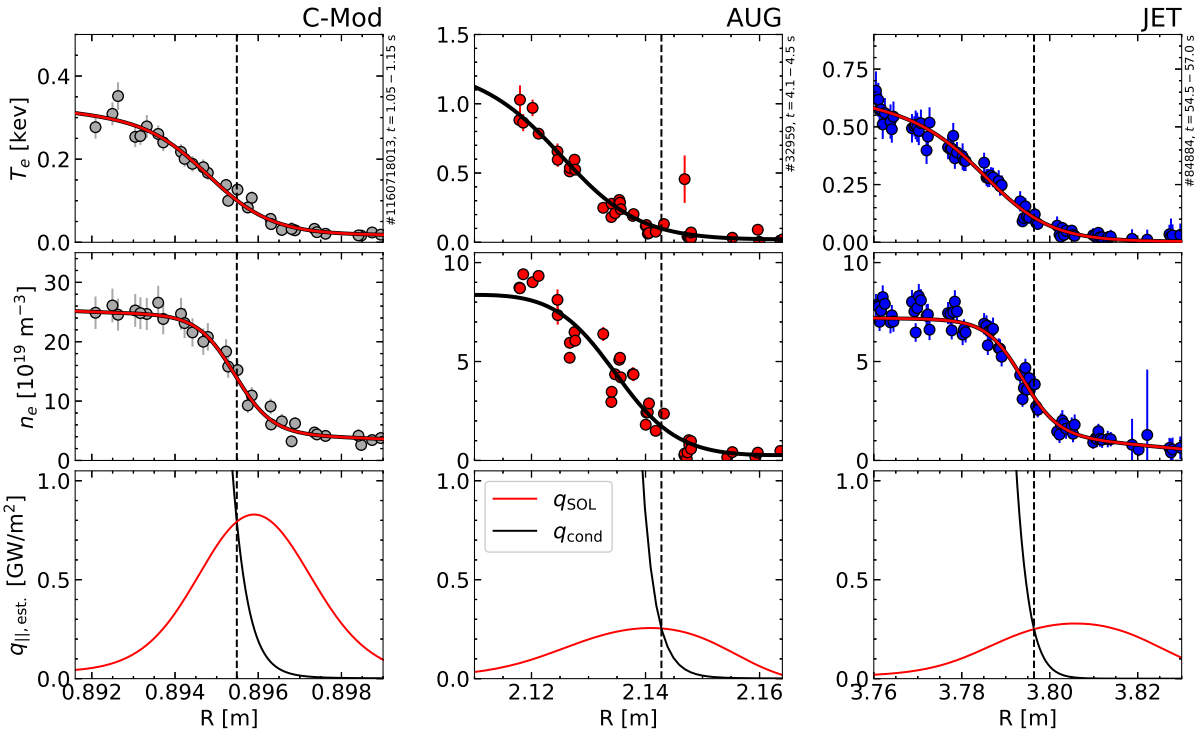

Figure 2: Example of H-mode electron temperature (top panels) and electron density (middle panels) edge profiles measured by the TS system in C-Mod (left), AUG (center) and JET (right). Data are plotted versus the outer midplane major radius and fit with a modified hyperbolic tangent function (solid lines). Bottom panels: radial profile of the parallel heat flux transported by electron conduction to the target $q_{e,||,\mathrm{cond}}$ (black) and radial profile of the estimated heat flux entering the SOL and being transported to the outer target $q_{e,||,\mathrm{SOL}}$ (red). The separatrix position (dashed vertical line) is defined where $q_{e,||,\mathrm{SOL}} = q_{e,||,\mathrm{cond}}$.

a vertical camera is employed, providing $P_{r,\mathrm{sep}}$ estimates within $\pm 10\,\%$ of the tomographic values. In C-Mod, $P_{r,\mathrm{sep}}$ is determined via Abel inversion of brightness measurements from a 16-channel resistive bolometer array, assuming flux surface symmetry [32]. When this reconstruction is not available, $P_{r,\mathrm{sep}}$ is estimated using a wide-angle resistive bolometer system, which provides the radiated power within the main chamber. The impact of $P_{r,\mathrm{sep}}$ uncertainties on the estimated separatrix values is discussed in section 3.

In this study, the main diagnostic used to measure the edge electron density and temperature is the Thomson scattering (TS) system, which probes both quantities from the same scattering volume. For ELMy H-modes, data have been collected between 75% and 95% of the ELM cycle to carry out SOL power balance analysis only during the quasi-stationary plasma phase before the ELM crash. Conversely, in EDA H-modes, all TS measurements within the time window of interest have been considered. The selected data have been mapped to the outer midplane and fit with a modified hyperbolic tangent function [33], with inner and outer linear polynomials, see Fig. 2.

As outlined in the introduction, the separatrix position is evaluated via SOL power balance.

The heat flux entering the SOL and being transported by electron conduction to the outer target, $q_{e,||,\mathrm{SOL}}$, is:

$$q_{e,||,\mathrm{SOL}} = \frac{P_{e,\mathrm{out,SOL}}}{A_{\mathrm{SOL}}} = \frac{f_{\mathrm{out}} f_{\mathrm{cond}} f_e P_{\mathrm{SOL}}}{A_{\mathrm{SOL}}}, \tag{1}$$

where $P_{e,\mathrm{out,SOL}}$ is the power entering the SOL and being transported by electron conduction to the outer target and A_{SOL} is the SOL cross-sectional area given by

$$A_{\mathrm{SOL}} = 2\pi R_{\mathrm{omp}} \lambda_{q,\mathrm{omp}} \frac{B_{p,\mathrm{omp}}}{B_{t,\mathrm{omp}}}, \tag{2}$$

where R is the major radius, B_p and B_t are the poloidal and toroidal magnetic field, respectively, and the subscript 'omp' stands for quantities evaluated at the outer midplane. In Eq. 1, f_{out}, f_{cond} and f_e represent the fraction of power carried to the outer target, the fraction of conducted power and the fraction of power transported by electrons, respectively. This heat flux is assumed to be entirely transported by electron conduction to the target, with no power sources or sinks, which is a valid assumption for attached or weakly detached plasmas. According to Spitzer-Härm conductivity, the parallel heat flux transported by electron conduction, $q_{e,||,\mathrm{cond}}$, is given by:

$$q_{e,||,\mathrm{cond}} = \frac{2}{7} \frac{\kappa_0 T_{e,\mathrm{sep}}^{7/2}}{L_{\mathrm{SOL}}}, \tag{3}$$

where κ_0 is the parallel electron conductivity coefficient, evaluated with the effective ion charge Z_{eff} correction $\kappa_0 = 2600/(0.672 + 0.076\sqrt{Z_{\mathrm{eff}}} + 0.252 \cdot Z_{\mathrm{eff}})\,\mathrm{W\,m^{-1}\,eV^{-7/2}}$ [2]. Equation 3 is obtained assuming that the separatrix electron temperature is much larger than the outer target electron temperature, $T_{e,\mathrm{sep}} \gg T_{e,\mathrm{tar}}$, which is a valid assumption in sufficiently collisional H-mode plasmas. From Eq. 1 and Eq. 3 a handy expression for the separatrix electron temperature can be derived:

$$T_{e,\mathrm{sep}} = \left(\frac{7 f_{\mathrm{out}} f_{\mathrm{cond}} f_e P_{\mathrm{SOL}} B_{t,\mathrm{omp}} L_{\mathrm{SOL}}}{4\pi R_{\mathrm{omp}} \kappa_0 \lambda_{q,\mathrm{omp}} B_{p,\mathrm{omp}}} \right)^{2/7}. \tag{4}$$

In this work, $f_{\mathrm{out}} = 0.65$ for AUG and JET [34], while $f_{\mathrm{out}} = 0.5$ for C-Mod [35, 36]. The remaining power fractions, f_{cond} and f_e, are both set to 0.8. These values have been obtained by comparing $T_{e,\mathrm{sep}}$ estimates from the 2-point model to those derived from a large database of EMC3-EIRENE simulations, in which density, heating power and transport coefficients were varied systematically [37]. The impact of f_{cond} and f_e uncertainties on the separatrix parameters will be discussed in section 3.

The SOL connection length between the outer midplane and the outer target has been calculated from the magnetic field line at approximately half $\lambda_{q,\mathrm{omp}}$, specifically from the major radius position at the outer midplane, located 1 mm from the separatrix in JET and AUG, and 0.5 mm from the separatrix in C-Mod.

The effective ion charge is a challenging quantity to measure at the separatrix, and in this work it is assumed to be 1.5 [16]. The impact of Z_{eff} uncertainty on $n_{e,\mathrm{sep}}$ will be discussed

in section 3.
The SOL power decay length at the outer midplane is evaluated according to the Spitzer-Härm assumption $\lambda_{q,\mathrm{omp}} = 2/7\lambda_{T_e}$, where $\lambda_{T_e} = |T_e/\nabla T_e|$ is the electron temperature decay length evaluated from the TS fit. Since we carried out a mtanh fit over the whole pedestal, a radial profile of λ_{T_e}, and hence λ_q, is obtained. As a consequence, both $q_{||,e,\mathrm{SOL}}$ and $q_{e,||,\mathrm{cond}}$ vary radially. Therefore, the separatrix position is determined by finding the root of the equation $q_{||,e,\mathrm{SOL}} - q_{e,||,\mathrm{cond}} = 0$, as shown in the bottom panels of Fig. 2 for each tokamak. It is instructive to note that the smallest device (C-Mod) is the one with the highest parallel heat flux entering the SOL; indeed, as size decreases for a fixed $P_{\mathrm{SOL}}/(\lambda_q B_{p,\mathrm{omp}}/B_{t,\mathrm{omp}})$, the power exhaust challenge significantly intensifies [38].
The deviation between the separatrix location at the outer midplane determined by this power balance analysis and magnetic equilibrium is discussed in Appendix A.

2.1. Evaluation of inter-ELM dW/dt

Figure 3 shows an example of how the inter-ELM $\mathrm{d}W_{\mathrm{MHD}}/\mathrm{d}t$ is evaluated in both JET and AUG. This methodology builds upon the one previously employed in Ref. [39] and relies on a fast equilibrium reconstruction, with time resolution of 2.5 kHz in JET and 10 kHz in AUG. First, a low pass filter is applied to the W_{MHD} signal to reduce noise on the temporal derivative. Second, the time derivative is evaluated, and data are selected only in the inter-ELM phase of interest (75-95% of the ELM cycle). A time smoothing of this signal is carried out with a moving Gaussian window of about the energy confinement time τ_E, before taking the average of the signal.
While in AUG the pick-up coils from which the equilibrium is reconstructed are located inside the vessel, in JET they are located outside the vessel. As a consequence, in the 20 ms after the ELM crash at JET an artificial increase of $\mathrm{d}W_{\mathrm{MHD}}/\mathrm{d}t$ is observed, which is due to the ELM induced currents in the vessel. Therefore, this methodology can be reliably applied at JET only for ELM frequency $f_{\mathrm{ELM}} < 40$ Hz, while at AUG the upper limit is given by the equilibrium time resolution (10 kHz).
Figure 3 shows that the inter-ELM $\mathrm{d}W_{\mathrm{MHD}}/\mathrm{d}t$ is not negligible in both devices. To be more quantitative in Fig. 4 the fraction of $\mathrm{d}W_{\mathrm{MHD}}/\mathrm{d}t$ over the absorbed heating power is plotted against the ELM frequency for both tokamaks. For the sake of generality, only for this figure the analysis of JET data has been expanded to the whole EUROfusion pedestal database, including also vertical-corner (VC) and vertical-horizontal (VH) target configurations [18]. Across a large range of plasma currents, plasma shapes, line-average density etc., this ratio is always between 0.1 and 0.4 both in JET and AUG, with average value being $\mathrm{d}W_{\mathrm{MHD}}/\mathrm{d}t = 0.25P_{\mathrm{abs}}$. This result is consistent with previous studies which found the ELM energy loss ΔW_{ELM} to obey the relation $\Delta W_{\mathrm{ELM}} f_{\mathrm{ELM}} = c \cdot P_{\mathrm{abs}}$, with c being a constant ranging between 0.2 and 0.4 [40, 41]. Assuming that after the ELM crash $\mathrm{d}W_{\mathrm{MHD}}/\mathrm{d}t$ is increasing linearly, $\Delta W_{\mathrm{ELM}} f_{\mathrm{ELM}} = \Delta W_{\mathrm{ELM}}/\Delta t_{\mathrm{ELM}} \approx \mathrm{d}W_{\mathrm{MHD}}/\mathrm{d}t = c \cdot P_{\mathrm{abs}}$, which is exactly what we have found.
Given the apparent generality of this relation, in this work it is assumed that $\mathrm{d}W_{\mathrm{MHD}}/\mathrm{d}t = 0.25P_{\mathrm{abs}}$ for $f_{\mathrm{ELM}} > 40$ Hz at JET. Analysis of ELM energy losses evaluated from kinetic profiles at high-ELM frequency at JET [42] confirmed the validity of this assumption.

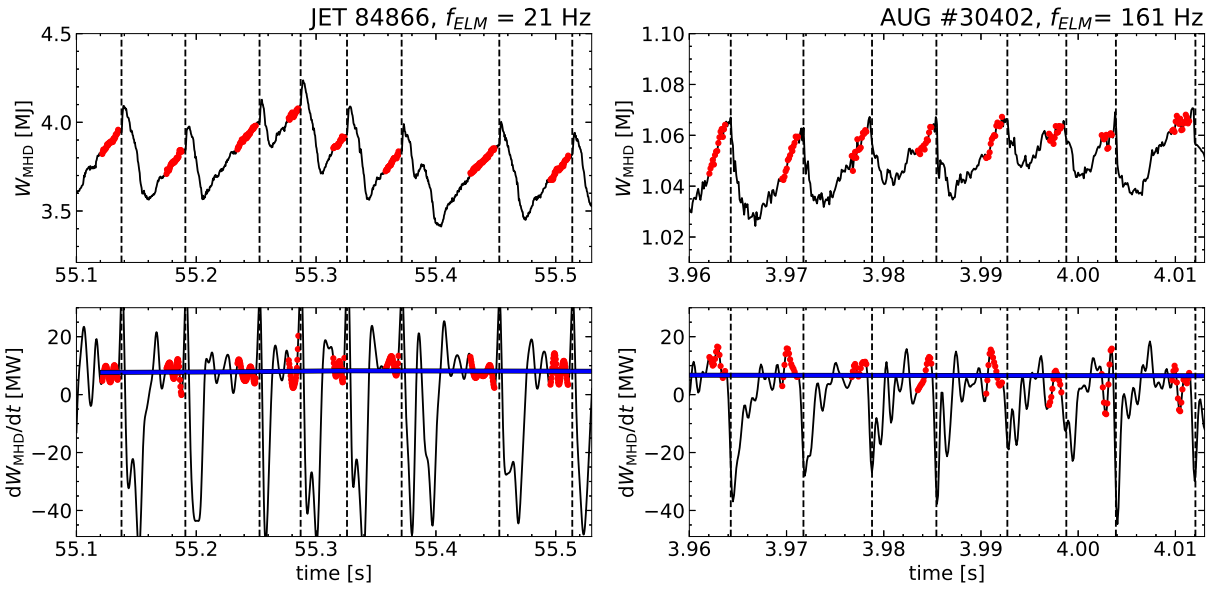

Figure 3: Top panels: Plasma stored energy evaluated from a high time resolution equilibrium reconstruction in JET (left) and AUG (right). Selected inter-ELM phases are highlighted in red. Bottom panels: Time derivative of the plasma stored energy $\mathrm{d}W_{\mathrm{MHD}}/\mathrm{d}t$, with selected inter-ELM phases highlighted in red. The blue line is a time smoothing of the selected inter-ELM $\mathrm{d}W_{\mathrm{MHD}}/\mathrm{d}t$. For more details refer to the text.

3. Sensitivity analysis on input parameters

In this section, the relative change of the separatrix electron density depending on varying input parameters is discussed. Figure 5 (a) shows the relative change of $n_{e,\mathrm{sep}}$ when the inter-ELM $\mathrm{d}W/\mathrm{d}t$ is set to zero. Since the H-mode phases under-analysis are stationary, this assumption is equivalent to evaluating an average $\mathrm{d}W/\mathrm{d}t$ over the whole time window. Neglecting the inter-ELM $\mathrm{d}W/\mathrm{d}t$ results in an increase in $n_{e,\mathrm{sep}}$ of up to 15 % in AUG and 25 % in JET. This change is due to the increase of P_{SOL}, and hence $T_{e,\mathrm{sep}}$, which occurs when the inter-ELM $\mathrm{d}W/\mathrm{d}t$ is neglected. The AUG discharges with no variation in $n_{e,\mathrm{sep}}$ are stationary H-mode phases without ELMs, where $\mathrm{d}W/\mathrm{d}t \approx 0$.

Figure 5 (b) shows the relative change of $n_{e,\mathrm{sep}}$ when the outer midplane $\lambda_{q,\mathrm{omp}}$ is evaluated from scaling laws instead of through the formula $\lambda_{q,\mathrm{omp}} = 2/7\lambda_{T_e}$. The Eich scaling law is used for AUG and JET [43], while the Brunner scaling law is employed for C-Mod [44]. When the $\lambda_{q,\mathrm{omp}}$ prediction from the scaling law is used, $n_{e,\mathrm{sep}}$ varies mildly in AUG (typically less than 10 %), while it changes up to 20 % in C-Mod, or up to 30 % in JET. The $\lambda_{q,\mathrm{omp}}$ deviation from the scaling law at AUG and JET could be due to a physics-based broadening at higher collisionality [45], whereas in C-Mod the $\lambda_{q,\mathrm{omp}}$ prediction from the scaling is always approximately a factor of two larger than $\lambda_{q,\mathrm{omp}} = 2/7\lambda_{T_e}$, as also previously found in Ref. [20].

In Fig. 5 (c) the impact of an approximated SOL connection length estimation on the separatrix density is explored. A typical approximation for the SOL connection length is

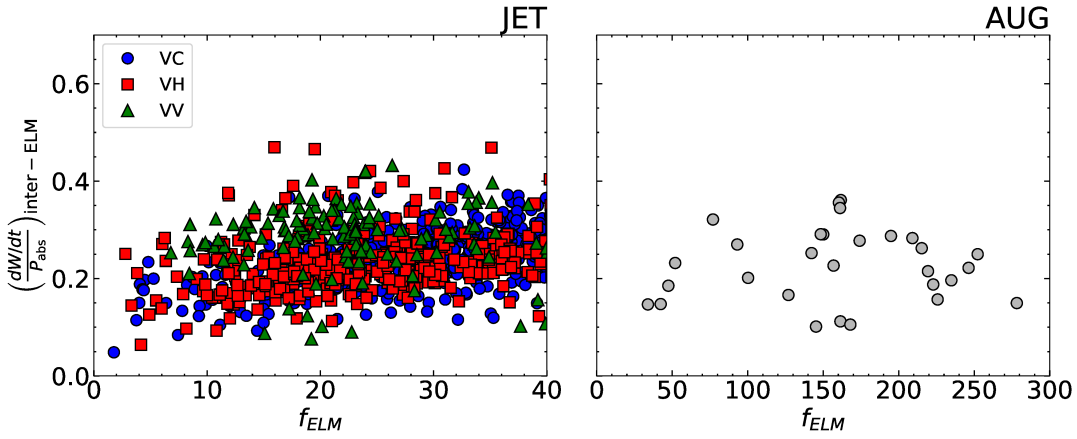

Figure 4: Ratio of the inter-ELM $\mathrm{d}W_{\mathrm{MHD}}/\mathrm{d}t$ and the absorbed heating power against ELM frequency for JET (left) and AUG (right). On JET, 'VC', 'VH' and 'VV' stand for the vertical-corner, vertical-horizontal and vertical-vertical target configurations, respectively, see e.g. [18].

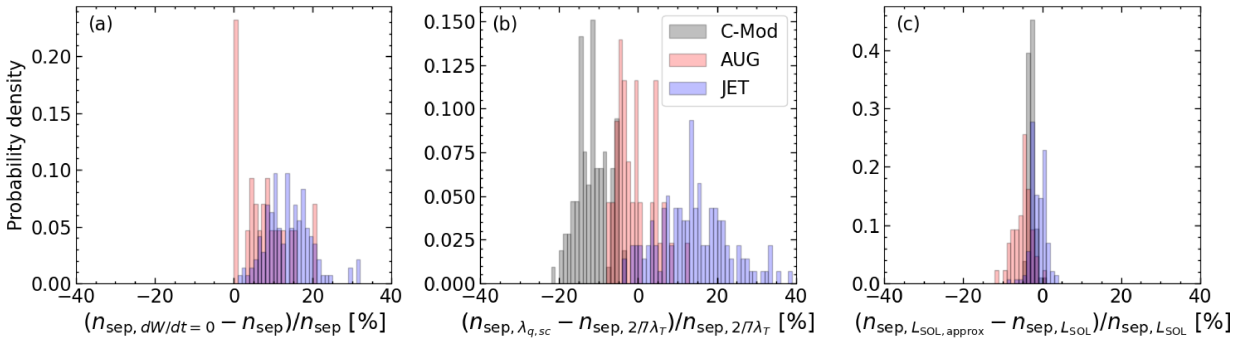

Figure 5: Probability density of relative change of $n_{e,\mathrm{sep}}$ when $\mathrm{d}W/\mathrm{d}t$ (a), $\lambda_{q,\mathrm{omp}}$ (b) and L_{SOL} (c) are varied in C-Mod (gray), AUG (red) and JET (blue). For more details on varied quantities refer to the text.

$L_{\mathrm{SOL,approx}} = \pi R_{\mathrm{geo}} q_{\mathrm{cyl},\delta}$, where R_{geo} is the geometrical major radius and $q_{\mathrm{cyl},\delta}$ is the edge safety factor evaluated from the cylindrical approximation and using a correction formula for the elongation to include the triangularity effect into account: $q_{\mathrm{cyl},\delta} = \frac{B_{\mathrm{t}}}{\langle B_{\mathrm{p}} \rangle} \frac{\hat{\kappa}}{A}$, with $A = R/a$ being the aspect ratio, $\langle B_{\mathrm{p}} \rangle = \frac{\mu_0 I_p}{2\pi a \hat{\kappa}}$ the average poloidal magnetic field and $\hat{\kappa} = \sqrt{(1 + \kappa^2(1 + 2\delta^2 - 1.2\delta^3))/2}$ [46]. It is worth noting that the ratio $L_{\mathrm{SOL,approx}}/L_{\mathrm{SOL}}$ is approximately constant for each device, being ~ 1.3 in AUG, ~ 1.17 in C-Mod and ~ 1 in JET. As a consequence, the induced variation in $n_{e,\mathrm{sep}}$ is mild, namely up to 5 % in JET and C-Mod, and up to 10 % in AUG, see Fig. 5 (c). It should be stressed, however, that the discrepancy between $L_{\mathrm{SOL,approx}}$ and L_{SOL} increases when the triangularity correction in $\hat{\kappa}$ is not considered, namely when $\hat{\kappa} = \sqrt{(1 + \kappa^2)/2}$ is employed.

A similar sensitivity analysis was carried out on $P_{r,\mathrm{sep}}$, f_{cond} and Z_{eff}. Both a 20 % increase in $P_{r,\mathrm{sep}}$ and a change of f_{cond} from 0.8 to 0.6 caused an approximate 5 % reduction in $n_{e,\mathrm{sep}}$ on

average. Conversely, changing $Z_{\rm eff}$ from 1.5 to 2.5 led to an average increase in $n_{e,\rm sep}$ of about 5 %. Thus, while this sensitivity analysis showed that uncertainties in $L_{\rm SOL}$, $P_{r,\rm sep}$, $f_{\rm cond}$ or $Z_{\rm eff}$ have little impact on the separatrix density value, it also underscored the importance of accurately evaluating $\lambda_{q,\rm omp}$ and the inter-ELM $\mathrm{d}W/\mathrm{d}t$ to reduce errors in determining the separatrix position.

4. Correlation with engineering parameters

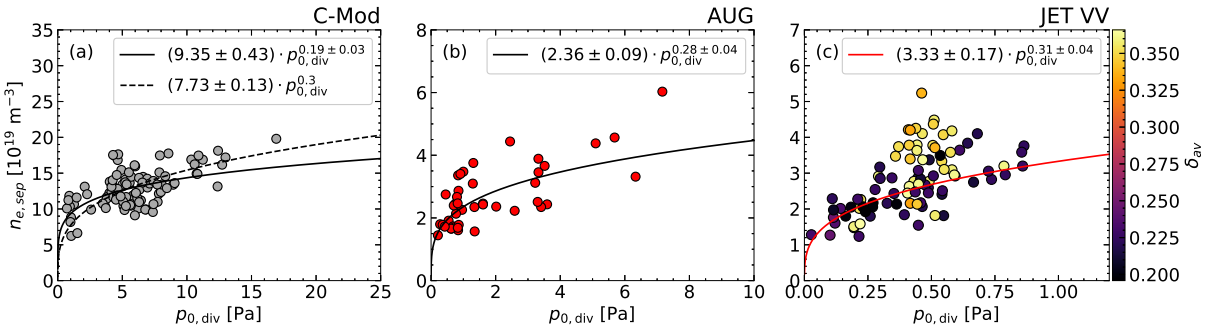

Figure 6: Electron separatix density versus the divertor neutral pressure in C-Mod (a), AUG (b) and JET (c). JET data have been color coded with the plasma average triangularity. Solid lines represent the result of a regression of the form $n_{e,\rm sep} = C \times p_{0,\rm div}^{\alpha}$, while the dashed line of the form $n_{e,\rm sep} = C \times p_{0,\rm div}^{0.3}$. The error of each derived coefficient is also displayed.

Fig. 6 shows the separatrix electron density against the divertor neutral pressure $p_{0,\rm div}$ for C-Mod, AUG and JET. The divertor neutral pressure is measured by a baratron located in the sub-divertor region. The measurement position is different in each device, being on a high-field side vertical port in AUG [15, 7], and on a low-field side vertical port in C-Mod [47] and JET [48], see figure 1. A positive correlation between these two quantities is found, namely when $p_{0,\rm div}$ rises $n_{e,\rm sep}$ increases. A regression of the type $n_{e,\rm sep} = C \times p_{0,\rm div}^{\alpha}$ is fit to the data of each device, with $p_{0,\rm div}$ being expressed in pascal. In AUG, the regression gives a normalized root mean square error nrmse = 26 % and an exponent of $\alpha = 0.28$, which is similar to the value previously found in [15]. In JET, the data used for the regression are from low-triangularity plasmas only. The JET exponent is $\alpha = 0.31$ (nrmse = 23 %), which is close to the AUG one. In C-Mod, the regression resulted in a slightly lower exponent $\alpha = 0.19$, with nrmse = 6 %. A regression of the form $n_{e,\rm sep} = C \times p_{0,\rm div}^{0.3}$ is also performed on C-Mod, which gives satisfactory agreement with data (nrmse = 17 %). Overall, all three devices exhibit a positive correlation between $n_{e,\rm sep}$ and $p_{0,\rm div}$ with exponents in the range 0.2–0.3.

In Fig. 6 (c), JET data have been color coded with the average plasma triangularity. It can be seen that for the same sub-divertor neutral pressure, plasmas with higher triangularity tend to have larger $n_{e,\rm sep}$ than plasmas with lower triangularity. Such behavior has been recently observed also in TCV [49], and could be due to several reasons, e.g. additional recycling coming from the main chamber or upper plate, a change in perpendicular transport or ELM

behaviour. Understanding the reasons of such dependency is beyond the scope of this work, however it is of high importance for extrapolations to ITER/DEMO-like plasma shapes, and should be pursued in the future.
The obtained dependency of $n_{e,\mathrm{sep}}$ with $p_{0,\mathrm{div}}$ is in line with 2-point model expectations, as previously outlined in [15]. Indeed, the recycling flux at the outer target is the driving physics mechanism setting the upstream separatrix density. This ion flux can be connected to the neutral density at the outer target, which, in turn, is proportional to the sub-divertor neutral pressure for a fixed divertor geometry in present day devices.

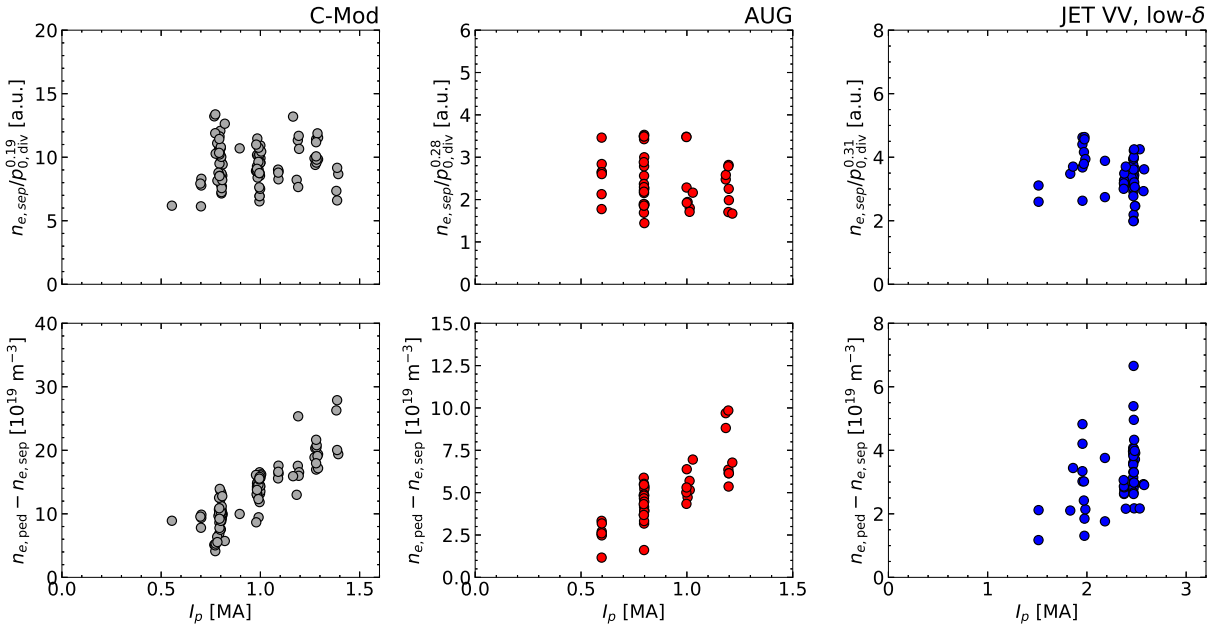

Figure 7: Top panels: Separatix electron density normalized to the divertor neutral pressure dependence found in each device versus the plasma current. Bottom panels: Difference between the pedestal top and separatrix electron density versus the plasma current in each tokamak.

Top panels of Fig. 7 show $n_{e,\mathrm{sep}}$ normalized to the divertor neutral pressure dependence versus the plasma current for each device. Across all the three devices, an almost absent dependence of $n_{e,\mathrm{sep}}$ on I_p is found. Again, this is in line with the 2-point model, which predicts a weak current dependence of $n_{e,\mathrm{sep}}$ [15]. It is worth noting that when $n_{e,\mathrm{sep}}$ is not normalized to the $p_{0,\mathrm{div}}$ dependence a weak correlation with the plasma current is obtained [15, 50]. This is because high-current operation typically requires an increased gas puff rate to sustain H-mode plasmas, which, in turn, leads to higher divertor neutral pressures [15, 51].
In the bottom panels of Fig. 7, the difference between the pedestal top and separatrix electron density $n_{e,\mathrm{ped}} - n_{e,\mathrm{sep}}$ is plotted against the plasma current for the three tokamaks. The pedestal top density has been evaluated at $\rho_{\mathrm{pol}} = 0.90$. In all three devices, the density increase between the pedestal bottom and pedestal top exhibits a marked dependence on plasma current. This finding is in line with the strong I_p dependence of the energy confinement time [52], and is the origin of the leading order scaling of pedestal top density

with I_p, reported for C-Mod [19, 53]. The combination of Fig. 7 and 6 highlights that the physics mechanism setting the electron density strongly varies across the (few-centimeters-wide) edge region of tokamak devices.

5. Conclusions

In this work, a multi-machine (C-Mod, AUG and JET) database of H-mode separatrix electron density has been assembled. The database construction employs exactly the same technique to evaluate the separatrix position in each device: The same fitting function has been applied to Thomson scattering data, and SOL power balance has been implemented identically on each tokamak. Moreover, the inter-ELM $\mathrm{d}W/\mathrm{d}t$ has been evaluated experimentally in JET and AUG and is found to be approximately a constant fraction of the absorbed heating power, $\mathrm{d}W/\mathrm{d}t \approx 0.25 P_{\mathrm{abs}}$.
A sensitivity analysis on the deduced $n_{e,\mathrm{sep}}$ values revealed that neglecting the inter-ELM $\mathrm{d}W/\mathrm{d}t$ or using λ_q values from scaling laws significantly affects the inferred $n_{e,\mathrm{sep}}$. On the other hand, uncertainties in SOL connection length, Z_{eff}, radiated power and fraction of conducted power have little impact on $n_{e,\mathrm{sep}}$.
The main finding of this study is that, across all devices, a similar relationship between $n_{e,\mathrm{sep}}$ and the divertor neutral pressure $p_{0,\mathrm{div}}$ is observed, namely $n_{e,\mathrm{sep}} \propto p_{0,\mathrm{div}}^{0.25\pm0.06}$. Additionally, upon normalizing $n_{e,\mathrm{sep}}$ to the obtained $p_{0,\mathrm{div}}$ dependency, no clear correlation with the plasma current is found. These observations align with the expected dependencies from the 2-point model [11, 12, 15], suggesting that in the present dataset, the upstream separatrix density is mainly set by recycling at the divertor target. On the other hand, the density increase between the pedestal bottom and the pedestal top strongly depends on plasma current across all devices, consistently with the strong I_p dependence of the confinement time. These findings highlight that the physics mechanism governing the electron density considerably varies across the narrow (few-centimeters-wide) steep gradient region of the tokamak edge.
In next-generation devices, such as ITER, higher neutral opacity is expected to make $n_{e,\mathrm{sep}}$ less sensitive to the divertor neutral pressure [54, 55]. Additionally, strong impurity seeding will be essential to reduce heat and particle loads. Therefore, expanding the current dataset to include high-opacity and high-seeding discharges will be crucial for reliable extrapolation to next-step devices.

Acknowledgment

The authors would like to thank E. Wolfrum for providing feedback to this manuscript. Fruitful discussion with D. Brida, E. Joffrin, O.J.W.F. Kardaun, B. LaBombard, G. Tardini and M.R.K. Wigram is also warmly acknowledged. This work has been carried out within the framework of the EUROfusion Consortium, funded by the European Union via the Euratom Research and Training Programme (Grant Agreement No 101052200 — EUROfusion). Views and opinions expressed are however those of the author(s) only and do not necessarily reflect those of the European Union or the European Commission. Neither

the European Union nor the European Commission can be held responsible for them. This work was supported by US DOE Awards DE-SC0014264, DE-SC0021629 and was published as part of the international project co-financed by the Polish Ministry of Science and Higher Education within the programme called 'PMW' for 2023-2024.

Appendix A. Deviation between the separatrix locations determined by power balance and magnetic equilibrium

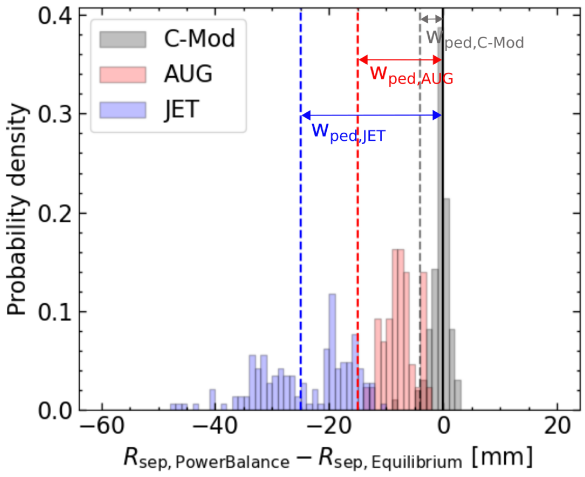

Figure A.8: Probability density of the deviation between the separatrix location determined by power balance analysis and magnetic equilibrium, for C-Mod (gray), AUG (red) and JET (blue). The separatrix location is measured at outer midplane major radius. Vertical dashed lines indicate the average pedestal width (in millimeters) for the three devices. The deviation between the separatrix location determined by power balance and the equilibrium can be substantial, even reaching the full pedestal width in some cases.

$R_{\mathrm{sep,PowerBalance}} - R_{\mathrm{sep,Equilibrium}}$

	C-Mod	AUG	JET
Mean (mm)	-0.6	-7.6	-24.1
Standard deviation (mm)	1.5	2.8	8.2
Minimum (mm)	-8.7	-13.5	-47.1
Maximum (mm)	2.8	-2.6	-10.0

Table A.2: Deviation between the separatrix location (outer midplane major radius) determined by power balance analysis and magnetic equilibrium for C-Mod, AUG and JET.

Figure A.8 shows the difference in the separatrix location at the outer midplane, as determined by power balance analysis on TS data and magnetic equilibrium, for the three tokamaks. In C-Mod, this deviation ranges from −2.1 mm to 0.9 mm on average (mean ± one standard deviation), with a minimum and maximum of −8.7 mm and 2.8 mm, respectively, as detailed in table A.2. In AUG, it varies on average between −10.4 mm and

−4.8 mm (with minimum and maximum values of −13.5 mm and 2.6 mm), whereas in JET it ranges from −3.2 cm to −1.6 cm on average (with extreme values of −4.7 cm and −1.0 cm). Several observations can be drawn from these data. First, across all devices, the magnetic equilibrium typically predicts the separatrix location to be shifted radially outward relative to the separatrix position given by power balance. Second, the deviation between the magnetically-reconstructed separatrix location and the one determined by power balance, which can serve as an indicator of the equilibrium uncertainty at the separatrix, increases with machine size. Specifically, the average deviation shifts from -0.6 mm in C-Mod, to -7.6 mm in AUG, and -2.4 cm in JET, as previously reported in Ref. [56, 57]. While this trend might suggest a size-dependent scaling of equilibrium uncertainty at the separatrix, it is important to note that machine-specific factors could significantly influence these results, cautioning against direct extrapolation to next-generation devices.
Third, in each device, this deviation is a considerable fraction of the pedestal width. Indeed, typical pedestal width values are between 2–6 mm in C-Mod [19], 1–2 cm in AUG [58], and 1–4 cm in JET [18, 59], with their average values displayed in Fig. A.8. In some cases, the deviation between the separatrix location determined by power balance and magnetic equilibrium can be even larger than the pedestal width itself.
Because of these deviations, edge TS data often need to be shifted radially to reconcile measurements from different diagnostics. For instance, in AUG, an 8 mm radial shift is typically applied to edge TS data [45, 60], in agreement with the average deviation reported in table A.2. In JET, the probability density distribution of this shift exhibits a double peak at approximately 3 cm and 1.8 cm, see Fig. A.8. This change in the statistical distribution of the shift occurred after several magnetic pick-up coils on the low-field-side were replaced between campaign 34 and 35 [56], highlighting the sensitivity of equilibrium uncertainty to the calibration accuracy of magnetic pick-up coils [61]. Lastly, it is important to note that the equilibria used in this analysis were determined using solely magnetic coil signals. Incorporating kinetic profile data into equilibrium evaluations typically enhances accuracy [56, 57, 61].

References

[1] KALLENBACH, A. et al., Plasma Physics and Controlled Fusion **58** (2016) 045013.
[2] GOLDSTON, R. J. et al., Plasma Physics and Controlled Fusion **59** (2017) 055015.
[3] REINKE, M. L. et al., Nuclear Fusion **57** (2017) 034004.
[4] FRASSINETTI, L. et al., Nuclear Fusion **61** (2021) 126054.
[5] DUNNE, M. G. et al., Plasma Physics and Controlled Fusion **59** (2017) 014017.
[6] HUGHES, J. et al., Nuclear Fusion **51** (2011) 083007.
[7] SILVAGNI, D. et al., Physics of Plasmas **31** (2024) 022501.
[8] LIPSCHULTZ, B. et al., Nuclear Fusion **24** (1984) 977.
[9] STROTH, U. et al., Nuclear Fusion **62** (2022) 076008.
[10] MANZ, P. et al., Nuclear Fusion **63** (2023) 076026.
[11] STANGEBY, P. C., Plasma Physics and Controlled Fusion **60** (2018) 044022.
[12] KRASHENINNIKOV, S. I. et al., Physics of Plasmas **23** (2016) 055602.
[13] LEONARD, A. et al., Nuclear Fusion **57** (2017) 086033.
[14] LOMANOWSKI, B. et al., Nuclear Fusion **63** (2023) 036019.
[15] KALLENBACH, A. et al., Plasma Physics and Controlled Fusion **60** (2018) 045006.

[16] STANGEBY, P. et al., Nuclear Fusion **55** (2015) 093014.
[17] STANGEBY, P., The Plasma Boundary of Magnetic Fusion Devices, Bristol: Institute of Physics Publishing, 2000.
[18] FRASSINETTI, L. et al., Nuclear Fusion **61** (2020) 016001.
[19] HUGHES, J. W. et al., Physics of Plasmas **9** (2002) 3019.
[20] BALLINGER, S. et al., Nuclear Fusion **62** (2022) 076020.
[21] SHIMADA, M. et al., Nuclear Fusion **47** (2007) S1.
[22] SICCINIO, M. et al., Fusion Engineering and Design **176** (2022) 113047.
[23] RODRIGUEZ-FERNANDEZ, P. et al., Nuclear Fusion **62** (2022) 042003.
[24] CHALLIS, C. et al., Nuclear Fusion **29** (1989) 563.
[25] MASLOV, M. et al., Nuclear Fusion **60** (2020) 036007.
[26] THOMSEN, K. et al., Nuclear Fusion **34** (1994) 131.
[27] CAVEDON, M., Power losses mechanisms for Neutral Beam injected particles in ASDEX Upgrade tokamak under different plasma configurations, Master thesis, University of Padua, 2012.
[28] BONOLI, P. T. et al., Fusion Science and Technology **51** (2007) 401.
[29] TOLMAN, E. et al., Nuclear Fusion **58** (2018) 046004.
[30] DAVID, P. et al., Nuclear Fusion **61** (2021) 066025.
[31] HUBER, A. et al., Fusion Engineering and Design **82** (2007) 1327.
[32] REINKE, M. L. and HUTCHINSON, I. H., Review of Scientific Instruments **79** (2008) 10F306.
[33] GROEBNER, R. et al., Nuclear Fusion **41** (2001) 1789.
[34] PITTS, R. et al., Journal of Nuclear Materials **337-339** (2005) 146.
[35] TERRY, J. et al., Journal of Nuclear Materials **438** (2013) S212 .
[36] BRUNNER, D. et al., Nuclear Fusion **58** (2018) 076010.
[37] BRIDA, D. et al., in preparation (2024).
[38] KUANG, A. Q. et al., Journal of Plasma Physics **86** (2020) 865860505.
[39] FIELD, A. R. et al., Plasma Physics and Controlled Fusion **62** (2020) 055010.
[40] HERRMANN, A. et al., Journal of Nuclear Materials **313-316** (2003) 759 .
[41] LOARTE, A. et al., Plasma Physics and Controlled Fusion **44** (2002) 1815.
[42] FRASSINETTI, L. et al., Nuclear Fusion **63** (2023) 112009.
[43] EICH, T. et al., Phys. Rev. Lett. **107** (2011) 215001.
[44] BRUNNER, D. et al., Nuclear Fusion **58** (2018) 094002.
[45] EICH, T. et al., Nuclear Fusion **60** (2020) 056016.
[46] UCKAN, N. A. and ITER Physics Group, ITER physics design guidelines: 1989, International Atomic Energy Agency (IAEA), 1990.
[47] NIEMCZEWSKI, A. et al., Nuclear Fusion **37** (1997) 151.
[48] KRUEZI, U. et al., Journal of Instrumentation **15** (2020) C01032.
[49] STAGNI, A. et al., Nuclear Fusion **64** (2024) 026016.
[50] HARRISON, J. R. et al., Plasma Physics and Controlled Fusion (2024).
[51] LUDA, T. et al., Nuclear Fusion **60** (2020) 036023.
[52] ITER Physics Expert Group on Confinement and Transport et al., Nuclear Fusion **39** (1999) 2175.
[53] HUGHES, J. W. et al., Physics of Plasmas **13** (2006) 056103.
[54] PITTS, R. et al., Nuclear Materials and Energy **20** (2019) 100696.
[55] PSHENOV, A. A. et al., 26th PSI-conference proceeding, submitted to Nucl. Materials and Energy (2024).
[56] SZEPESI, G. et al., 47th EPS Conf. on Plasma Physics (2021), P3.1037 .
[57] MORALES, R. B. et al., Review of Scientific Instruments **95** (2024) 043501.
[58] SCHNEIDER, P. A. et al., Plasma Physics and Controlled Fusion **54** (2012) 105009.
[59] BEURSKENS, M. N. A. et al., Plasma Physics and Controlled Fusion **51** (2009) 124051.
[60] FISCHER, R. et al., Fusion Science and Technology **58** (2010) 675.
[61] FISCHER, R. et al., Fusion Science and Technology **76** (2020) 879.